JGR Space Physics

RESEARCH ARTICLE
10.1029/2019JA027683

Saturn's Auroral Field-Aligned Currents: Observations From the Northern Hemisphere Dawn Sector During Cassini's Proximal Orbits

G. J. Hunt[1], E. J. Bunce[2], H. Cao[3,4], S. W. H. Cowley[2], M. K. Dougherty[1], G. Provan[2], and D. J. Southwood[1]

[1]Blackett Laboratory, Imperial College London, London, UK, [2]Department of Physics and Astronomy, University of Leicester, Leicester, UK, [3]Department of Earth and Planetary Sciences, Harvard University, MA, USA, [4]Division of Geological and Planetary Sciences, California Institute of Technology, CA, USA

Key Points:
- We analyze the northern hemisphere auroral field-aligned currents at dawn observed during Cassini's Proximal orbits
- We separate the planetary period oscillation (PPO) currents from PPO-independent currents and determined their current sheet properties
- Comparing the Proximal and F-ring observations, we show the PPO-independent's upward current is stronger at dawn compared to near noon

Correspondence to:
G. J. Hunt,
g.hunt@imperial.ac.uk

Citation:
Hunt, G. J., Bunce, E. J., Cao, H., Cowley, S. W. H., Dougherty, M. K., Provan, G., & Southwood, D. J. (2020). Saturn's auroral field-aligned currents: Observations from the northern hemisphere dawn sector during Cassini's Proximal orbits. *Journal of Geophysical Research: Space Physics*, *125*, e2019JA027683. https://doi.org/10.1029/2019JA027683

Received 28 NOV 2019
Accepted 31 MAR 2020
Accepted article online 14 APR 2020

Abstract We examine the azimuthal magnetic field signatures associated with Saturn's northern hemisphere auroral field-aligned currents observed in the dawn sector during Cassini's Proximal orbits (April 2017 and September 2017). We compare these currents with observations of the auroral currents from near noon taken during the F-ring orbits prior to the Proximal orbits. First, we show that the position of the main auroral upward current is displaced poleward between the two local times (LTs). This is consistent with the statistical position of the ultraviolet auroral oval for the same time interval. Second, we show the overall average ionospheric meridional current profile differs significantly on the equatorward boundary of the upward current with a swept-forward configuration with respect to planetary rotation present at dawn. We separate the planetary period oscillation (PPO) currents from the PPO-independent currents and show their positional relationship is maintained as the latitude of the current shifts in LT implying an intrinsic link between the two systems. Focusing on the individual upward current sheets pass-by-pass, we find that the main upward current at dawn is stronger compared to near noon. This results in the current density being ~1.4 times higher in the dawn sector. We determine a proxy for the precipitating electron power and show that the dawn PPO-independent upward current electron power is ~1.9 times higher than at noon. These new observations of the dawn auroral region from the Proximal orbits may show evidence of an additional upward current at dawn likely associated with strong flows in the outer magnetosphere.

1. Introduction

Electrical currents that flow along magnetic field lines are fundamental in the transfer of angular momentum between an ionosphere and a planetary magnetosphere. These currents are known as field-aligned currents. In the case of Saturn, there have been extensive studies of the auroral field-aligned currents using the azimuthal magnetic field component as measured by the magnetometer onboard the Cassini spacecraft (Bradley et al., 2018; Bunce et al., 2008; Dougherty et al., 2004; Hunt et al., 2014, 2015, 2016, 2018; Southwood & Kivelson, 2007; Talboys et al., 2009a; Talboys et al., 2009b; Talboys et al., 2011). Saturn's auroral field-aligned currents have been observed to be comprised of three large-scale systems, the first is a quasi-static axisymmetric system associated with the shear in angular velocity in the outer magnetosphere, close to the open-closed field line boundary (OCB) (Cowley et al., 2004; Cowley et al., 2008). The other two large-scale current systems rotate with the two planetary period oscillation (PPO) periods that pervade Saturn's magnetosphere (Andrews et al., 2011; Carbary & Mitchell, 2013; Gurnett et al., 2009). Specifically, these rotating currents through Ampère's law produce the PPO perturbation fields that are omnipresent within the Saturnian system (Andrews et al., 2010; Provan et al., 2009; Southwood & Cowley, 2014; Southwood & Kivelson, 2007).

The current systems introduced above have been described in detail by Bradley et al. (2018) and Hunt et al. (2014, 2015) such that only the key aspects will be repeated here. These papers contain diagrams of the current systems described below. The large-scale quasi-static axisymmetric system is independent of the PPOs such that we will refer to this current as the PPO-independent system. It is formed of a distributed downward current within the open polar cap region, which closes within the ionosphere as an equatorially directed horizontal meridional current leading to an axisymmetric ring of upward field-aligned current just

equatorward of the OCB. The upward current maps into the magnetosphere closing as a radially outward current within the magnetospheric plasma (Cowley et al., 2008; Cowley, Bunce, & O'Rourke, 2004). The PPO currents, on the other hand, are directed in opposite directions on either side of the polar region and rotate with the northern and southern PPO rotation periods. The general form of these current systems is into the ionosphere (as a downward current) on one side of the planet, across the polar cap in the ionosphere and out of the ionosphere (as an upward current) on the other side of the planet. The current then closes partly in the magnetospheric plasma and partly in the auroral region in the opposite hemispheres (Hunt et al., 2015). Bradley et al. (2018) showed that this split was approximately 50% during Saturn's northern spring in 2013. Two of these systems have been shown to the present within Saturn magnetosphere, one is associated with the northern PPOs and the other with the southern PPOs (Andrews et al., 2010; Hunt et al., 2014, 2015; Southwood & Kivelson, 2007). Here, we focus on the field-aligned currents and their closure in the ionosphere. During the final year of the Cassini mission, which we focus on here, the PPO periods were shown to be highly stable and to be ~10.79 hr for the northern system and ~10.68 hr for the southern (Provan et al., 2018).

By exploiting the difference in axial symmetry of the PPO-related and PPO-independent current systems, it is possible separate each contribution within the data. The main PPO field-aligned currents were shown to be approximately colocated with the main PPO-independent auroral field-aligned current and to be approximately equal in strength (Bradley et al., 2018; Hunt et al., 2014, 2015). The superposition of these three current systems acts to enhance or reduce the overall strength and form of the auroral field-aligned currents. Modulations of the ultraviolet and infrared auroral intensity and power has been shown to agree with the expected PPO modulated current (Bader et al., 2018; Badman et al., 2012; Kinrade et al., 2018; Carbary & Mitchell, 2013; Nichols et al., 2010, 2014). Moreover, the expected dual modulation of the aurora by both PPO systems due to the interhemispheric currents has recently been shown to be present (Bader et al., 2018; Hunt et al., 2015). In addition to the observed systems described above, there is a further proposed local time (LT) fixed system at dawn/dusk associated with the solar wind interactions and tail reconnection events (Cowley et al., 2004; Jackman & Cowley, 2006). In these proposed systems, the return flows in the dawn sector were the combination of the Dungey and Vasyliunas cycles return flows and resulted in enhanced flows in the outer dawn magnetosphere. Hunt et al. (2016) with a limited number of observations during the 2006–2008 high-latitude interval did not find evidence of such a current system. However, the final orbits of the Cassini mission crossed the northern auroral region within the dawn sector (06–08 hr LT), therefore allowing further exploration of this topic, and will be the main focus of this paper.

During Cassini's Proximal orbits, the spacecraft performed 22 highly inclined orbits that took it from the northern auroral region, between the planet's upper atmosphere and its inner rings, and to the southern auroral region within approximately 6 hr. The first magnetometer results from nine of those orbits were presented by Dougherty et al. (2018). Cao et al. (2019) presented a more detailed analysis of the entire proximal magnetometer data set, focusing on the internal planetary field. They showed that to explain the planetary magnetic field at periapsis, an axisymmetric 11-degree spherical harmonic model was required and that Saturn's dipole axis tilt must be less the 0.007° from the spin axis of the planet. In addition, a field-aligned current system was discovered to flow along field lines that thread the region inside the D-ring, Saturn's innermost ring (Dougherty et al., 2018; Hunt et al., 2019; Khurana et al., 2018; Provan et al., 2019). Recently, Provan et al. (2019) determined the PPO and mean residual field on the Proximal orbits from the auroral region to the gap between Saturn and the D-ring by performing sinusoidal fits to the data in bins of colatitude.

In Figure 1, we show magnetic field data for ±3 hr about periapsis in spherical polar coordinates from all 22 full Proximal orbits as color-coded at the top of the figure. Below the figure, an average of radial, latitude, and LT of the spacecraft is given. The radial (B_r) and meridional (B_θ) components (Figures 1a and 1b) are residual fields where the 11° model of Dougherty et al. (2018) has been subtracted. This model is axisymmetric such that $B_\varphi \equiv 0$.The large-scale morphology of these components can mostly be explained as contributions from the magnetospheric ring current. To show this, we overplot the B_r and B_θ fields from the Bunce et al. (2007) magnetospheric ring current model with the magnetopause standoff distance set to 22 R_S (Rs = 60268 km) as the dot-dashed black profiles. The smaller scale structures around periapsis imply contributions from below the spacecraft and could be higher order terms in the planetary magnetic field or ionospheric sources as discussed by Dougherty et al. (2018) and Provan et al. (2019). Figure 1c shows the azimuthal (B_φ) field

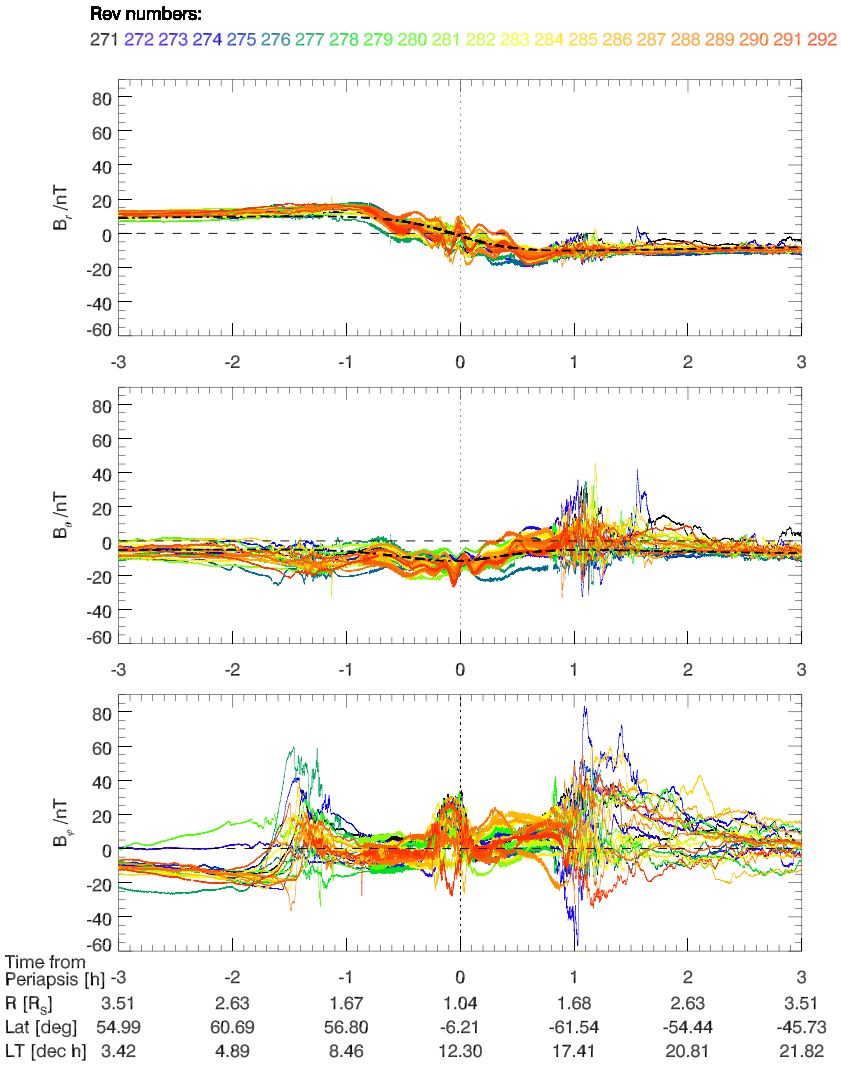

Figure 1. Overview of magnetic field data from the Proximal orbits (Revs 271–292) ±3 hr about periapsis, color-coded at the top of the figure. (a) The residual radial (B_r) component of the magnetic field, where we have subtracted the Dougherty et al. (2018) internal field model. (b) The residual meridional (B_θ) field component. The black dot-dashed profiles in panels (a) and (b) are the radial and meridional fields from a magnetospheric ring current model (Bunce et al., 2007). (c) The azimuthal (B_φ) field component. Below the figure, we give time relative to periapsis in hours, the radial distance of the spacecraft in Saturn radii (60268 km), together with the spacecraft latitude (deg) and LT (hr).

component as directly observed. Examining these data, the field-aligned current signatures are strikingly obvious. First, between ~2 and 1 hr prior to periapsis, Cassini crossed the northern auroral field-aligned currents between ~06 and 08 hr LT. Second, approximately 15 min prior to periapsis, centered about the magnetic equator and close to local noon is the intra-D ring current. Third, at ~1 hour after periapsis, Cassini entered the southern auroral field-aligned currents region at ~17–18 hr LT. The variability of the B_φ data for the remainder of the plot indicates that Cassini did not fully traverse the auroral field-aligned current region and traveled along or close to this region for some time, making it hard to identify the main current sheets. During the southern auroral region encounters, there were significant signatures in the B_θ component, which were not observed in the northern hemisphere to the same extent. This is likely due to Cassini traversing more in azimuth than in colatitude during the crossing of the southern auroral region; see Figure 2d. For the remainder of this paper, we will focus solely on the northern hemisphere currents. We will compare with the F-ring orbit observations to investigate if an enhancement of upward current, as previously expected, within the dawn sector related to return flows associated with large-scale

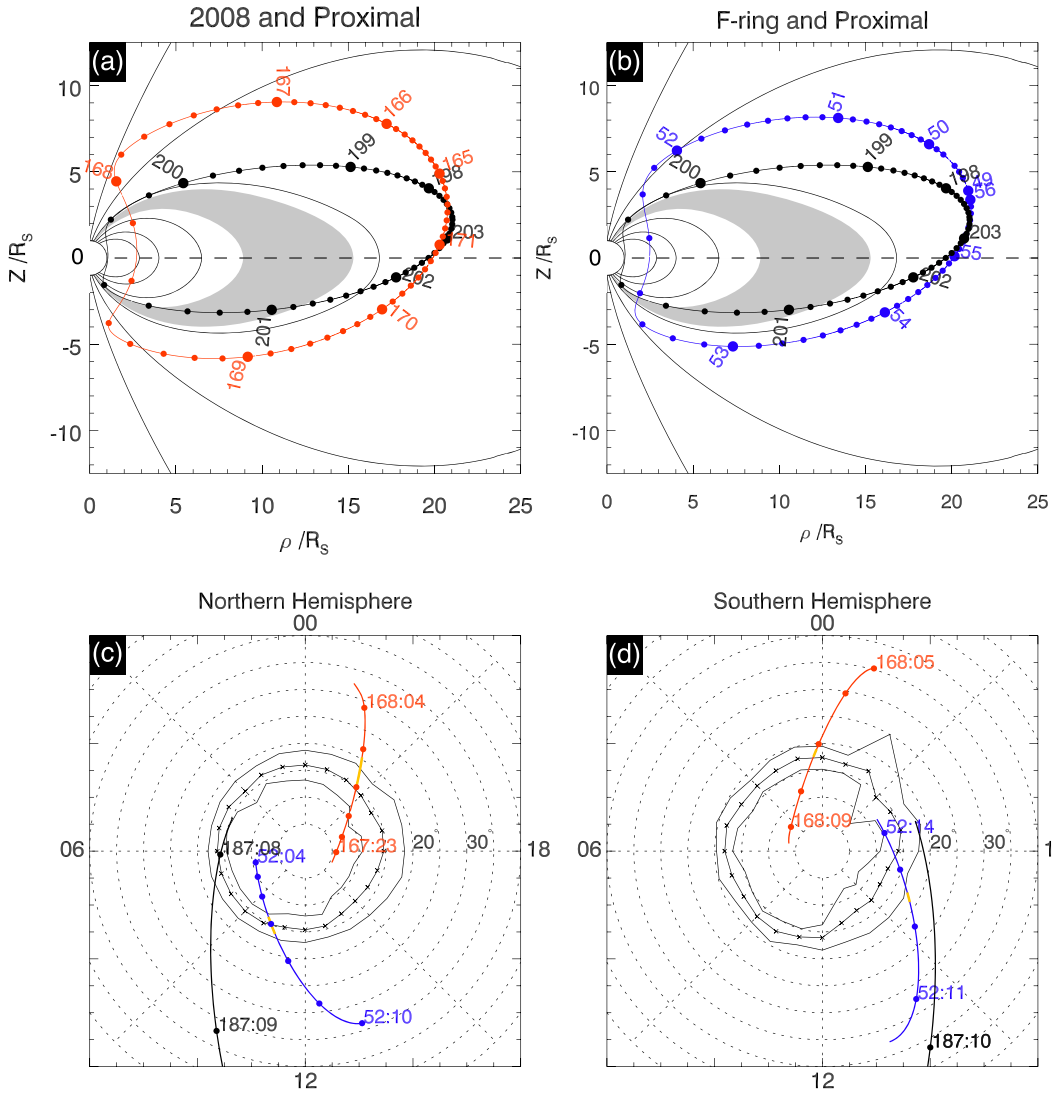

Figure 2. Comparison of Cassini trajectories plotted in the ρ-z plane, panels (a) and (b), and mapped in the northern and southern ionosphere, panels (c) and (d). (a) Comparison between a typical 2008 orbit (red) and Proximal orbit (black). Day of year markers are shown, and the circles are every 3 hr. The gray shaded region marks the typical field-aligned current region. Model field lines are shown, the model is comprised of a 3-degree planetary field and ring current. (b) Comparison between a typical F-ring (blue) and Proximal (black) orbit in the same format as panel (a). (c, d) Ionospheric projections using the field model as above and in text are plotted with circles shown at every hour, with DOY:hh labels at first and last hour markers, and the orange section shows the observed upward current regions. Both are viewed from the north. Orbits have the same coloring as in panels (a, b). Statistical auroral boundaries (solid lines) as defined by the half power emission and peak emission (crossed centerline) determined from Cassini Ultraviolet Imaging Spectrograph observations are shown (Carbary, 2012).

magnetospheric circulation patterns and magnetotail dynamics is present. We will show here that the observed PPO-independent upward current at dawn is stronger than at noon.

2. Data Set and Analysis Methodology

2.1. Data Set

In this study, we employ 1 s averaged measurements of the azimuthal magnetic field from Cassini's Proximal orbits during 2017, in particular, Revs 271–292, a Rev being an orbit of Cassini about Saturn timed from apoapsis to apoapsis. In Figure 2, we show a comparison between several high-latitude sequences of Cassini orbits, namely, the 2008 (Revs 59–95), F-ring (Revs 251–270), and Proximal orbits (Revs 271–292).

The first two sets have been studied in detail by Hunt et al. (2014, 2015, 2018), while the latter is the focus of this present study. Figure 2a shows the orbit geometries of Revs 72 (2008, red) and 284 (Proximal, black) in cylindrical (ρ,z) coordinates, where z is directed along the planet's spin/magnetic axis and ρ is the perpendicular distance from that axis. The large circles mark day of year, while the smaller circles are shown every 3 hr. Model magnetic field lines are shown together with a gray shaded region marking the expected location of the auroral field-aligned currents. We employed the first three terms of the Dougherty et al. (2018) Cassini 11 model together with the Bunce et al. (2007) magnetospheric ring current with the subsolar magnetopause standoff distance set at 22 R_S (Achilleos et al., 2008). Figure 2b shows the comparison between Revs 262 (F-ring, blue) and 284 (Proximal, black), also in cylindrical (ρ,z) coordinates. While the 2008 and F-ring orbits cross the field-aligned currents at approximately similar ρ values of 2 R_S, for the Proximal orbits, crossing occur closer to the planet at $\rho \sim 1$ R_s. The Proximal orbits' geometries also differ in their poleward extent. Inbound in the northern hemisphere, Cassini lay just poleward of the expected field-aligned currents, while outbound in the southern hemisphere, the Cassini spacecraft did not fully cross the expected field-aligned current regions as already noted, before traveling into the southern nightside plasma sheet. Instead, it traveled along or close to current carrying field lines for ~15 hr. This is supported by the data shown in Figure 1c.

Figures 2c and 2d show the polar projections of the Cassini magnetic footprint in the ionosphere for the orbits shown in Figures 2a and 2b in the northern and southern hemispheres, respectively. The spacecraft's magnetic footprint is determined from the same magnetic field model as shown in Figures 2a and 2b. The circles markers are every hour. We also show the average UV auroral boundaries from Carbary (2012) (see figure caption for details). The northern hemisphere projection shows the LT difference between the F-ring and Proximal orbit encounters with the expected auroral field lines. The Proximal orbits cross the auroral oval at ~06–08 hr LT while the F-ring orbits cross in the ~10–12 hr sector. The colatitude coverage in the polar region shows the F-ring orbits were ~5° more poleward than the Proximal trajectories with clear crossing of the auroral region. In the southern hemisphere, the LT coverage is approximately the same between the F-ring and Proximal orbit trajectories. Again, this shows that the Proximal orbits did not fully cut through all the auroral field lines, with Cassini being on field lines towards the equatorial edge of the auroral field lines, as inferred from the B_φ shown in Figure 1c. As shown in Figure1, the northern hemisphere FAC crossings have clear, dominant signatures in the φ component. Therefore, we feel this small change in LT during the northern hemisphere Proximal orbit crossings does not affect the comparison with other LTs, in particular the F-ring orbits which are the focus here. In addition, due to the short duration of the crossings, on the order of minutes to an hour for the Proximal and F-ring orbits, respectively, we can treat each crossing as a snapshot in time at approximately a constant PPO phase and PPO-related current strength.

2.2. Methodology

In this section, we give a brief outline of the methodology for analyzing the azimuthal (B_φ) component of the magnetic field in order to estimate the strength and structure of the field-aligned currents. We follow the same procedures as in Hunt et al. (2014), where full details are given.

To begin, we estimate the horizontal meridional current, I_m, that flows in the ionosphere at the base of the magnetic field lines, which turns off the azimuthal field perturbation due to the field-aligned currents in the atmosphere below the ionosphere. To do this, we take $\rho B_\varphi \approx$ constant along magnetic field lines in the region between closure currents in the ionosphere and the magnetosphere, a condition shown to be exact for the case of an axisymmetric field and to be approximately true for thin azimuthally extended field-aligned current sheet (see appendix B of Hunt et al. (2014)). The meridional horizontal ionospheric current, I_m, per radian of azimuth (MA/rad), is then determined by applying Ampère's law to a circular path through the observation point of radius ρ, giving

$$I_m = -\frac{\rho B_\varphi}{\mu_0}, \tag{1}$$

where $\mu_0$is the permeability of free space. This is defined such that a positive I_m is in the southward direction, that is, positive then directed equatorward in the northern hemisphere. Under the same assumption of weak azimuthal variations of the current, current continuity then requires that the total field-aligned current per

radian of azimuth flowing between two colatitude points, θ_1 and θ_2, such that $\theta_1$is poleward of θ_2 ($\theta_2 > \theta_1$), is given by

$$I_{\parallel} = -(I_m(\theta_2) - I_m(\theta_1)). \quad (2)$$

This is defined such that positive $I_{\parallel}$ means a field-aligned current directed parallel to the background magnetic field in the northern hemisphere and antiparallel to the field in the southern hemisphere.

Lastly, in order to analyze and separate the PPO and PPO-independent current contributions, we employ the local phases of the northern and southern PPO systems (Ψ_N,Ψ_S) given by

$$\Psi_{N,S}(\varphi, t) = \Phi_{N,S}(t) - \varphi. \quad (3)$$

Here, $\Phi_{N,S}(t)$ are the global PPO phases defined as the azimuthal angle from noon where the PPO perturbation equatorial quasi-uniform field points radially outwards from the planet at time t, and φ is the similarly defined azimuthal angle of the spacecraft. Both $\Phi_{N,S}(t)$ and φ are defined such that they increase from noon in the direction of planetary rotation (towards dusk). The global phases $\Phi_{N,S}(t)$ have been determined over the Proximal and F-ring orbit interval by Provan et al. (2018), who find that the northern and southern periods are near-constant at 10.792 hr for the northern system and 10.679 hr for the southern system, such that the global phases increase linearly in time at a rate corresponding to these periods. The calculated local phases $\Psi_{N,S}$ are thus a function of time and spacecraft azimuthal position, thereby giving the azimuthal location of the spacecraft relative to the rotating PPO field perturbations. We note that the PPO B_φ field perturbations at a fixed near-equatorial point are expected to vary as ~sin$\Psi_{N,S}$, while in the open polar field regions, this switches to ~ − sin$\Psi_{N,S}$.

3. Overview Comparison of Data

In this section, we average the northern ionospheric colatitude (θ_{iN}) profiles of meridional current (I_m) determined from the Proximal orbits. We then compare this to similarly calculated profiles from the 2008 (nightside) and the F-ring (noon) orbits to assess LT differences.

In Figure 3a, we show all the Proximal orbits northern I_m profiles as functions of θ_{iN}, each Rev being color-coded as shown at the top of the figure. While there is considerable orbit-to-orbit variability in these profiles, which is largely due to the contributions from the PPO-related current systems as well as dynamical changes in Saturn's magnetosphere, there is also a consistent large-scale form to the set of profiles. Examining these profiles from the polar (smaller) colatitudes towards more equatorial (larger) colatitudes, we see that typically the profiles are positive with a value ~1.1 MA/rad at θ_{iN} ~ 15°, indicative of a swept back (lagging) field with respect to planetary rotation. There is then a sudden negative gradient with colatitude, which from equation 2 is associated with a large field-aligned current ~1 MA/rad away from the planet parallel to the northern magnetic field lines centered at θ_{iN} ~16–17°. Between ~16° and 20°, the I_m values then become predominately negative, indicating a swept forward (leading) field with respect to planetary rotation. The current profiles then gradually return to positive values past θ_{iN} ~22°. Again, the spread in the profiles within this region can mostly be explained by the presence of the PPO-related perturbation fields modulating B_φ as ~sin($\Psi_{N,S}$) as shown by Provan et al. (2019). We will return to this later in the paper. The spike at θ_{iN} ~ 25.5° during Rev 291 is the crossing of the Enceladus flux tube as reported by Sulaiman et al. (2018). The Proximal orbits observations of the auroral field-aligned currents sampled approximately the full range of phases of the PPO cycles (Ψ_N,Ψ_S); if one then averages over the profiles, this will remove the PPO-related current contribution to a first approximation, thus leaving an estimate of the PPO-independent current. This averaged profile is shown by the joined black circles overplotted on the colored profile, where we have employed 1° colatitude bins which are spaced every 0.5° such that the bins overlap. The median values were also calculated but were found to be very similar to the mean values. The mean profile shown should be regarded as an approximation to the field-aligned current system, which is independent of the PPOs. Later in the paper, we will address this in more detail. We note here that Provan et al. (2019) determined a very similar profile (see their Figure 19b) via a different methodology. They performed sinusoidal fits to colatitudinally binned azimuthal field data, in which they determined the mean background field and show similar I_m values as shown here.

We compare the mean profile from the Proximal orbits with the similarly obtained profiles from other high-latitude orbits earlier in the mission. Figure 3b compares with the F-ring data obtain in the 6 months

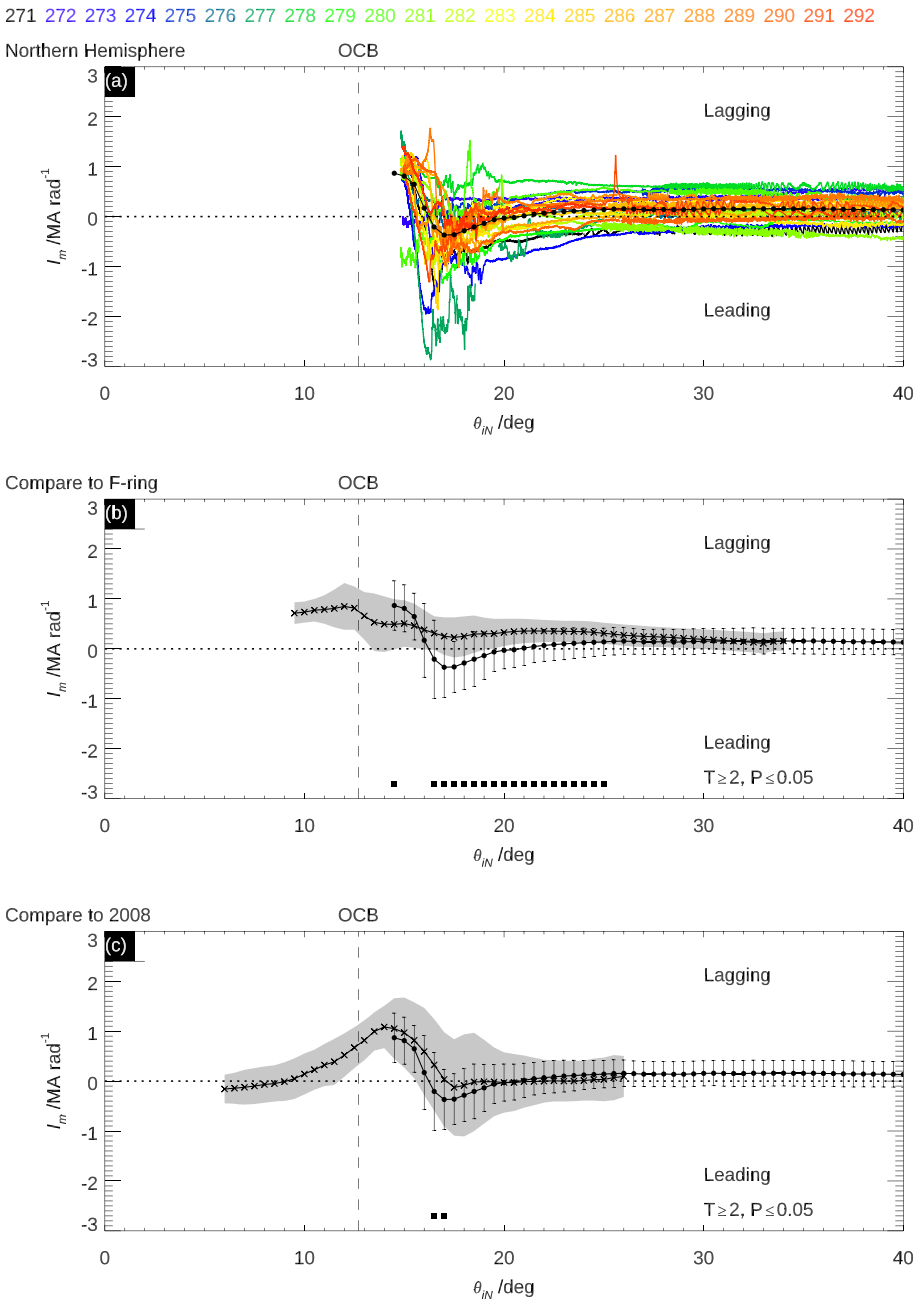

Figure 3. A statistical analysis of the northern colatitude (θ_{iN}) meridional horizontal ionospheric current (I_m) profiles. (a) Individual Proximal orbit colatitudinal I_m profiles color-coded by Rev number as shown at the top of the figure. The black circle profile is an average profile of 1° bins which overlap by 0.5°. Lagging and leading refer to the sense of the azimuthal field with respect to planetary rotation. (b) Comparison between the average profile from panel (a) shown by the jointed black circles, and the average profile from the F-ring orbits (Hunt et al., 2018) shown by the jointed crosses. The error bars show a standard deviation about the Proximal orbit mean profile as does the gray shaded region for the F-ring orbits. The filled black squares show the colatitude bins where the Welch's *T* test shows a significant difference between the two data sets means. (c) Similar format to panel (b) but comparing the mean profile from panel (a) with the mean profile of the 2008 data set (Hunt et al., 2015). The vertical dashed line shows the open-closed field line boundary from Jasinski et al. (2019).

prior to the Proximal orbits, which Figure 3c compares with the 2008 nightside northern hemisphere field-aligned current crossings. The joined black circles in both figures are the mean profile from Figure 3a, together with the standard deviations shown as error bars. The joined crosses show the F-ring

values in Figure 3b and 2008 values in Figure 3c from Hunt et al. (2015, 2018), where the gray regions show the standard derivation of the mean profiles.

Examining the profiles in Figure 3b, there is a significant difference between the northern F-ring and Proximal orbit field-aligned current observations. First, the form of the profiles differs considerably. In particular, in the main upward current region, the mean F-ring current profile is more gradual compared with the sharper profile from the Proximal orbit data, indicating a smaller field-aligned current density. Second, the F-ring mean I_m values are all positive (lagging field), whereas the Proximal mean I_m values have a clear negative peak at the base of the upward current (leading field) and are at least one standard deviation from the F-ring means. Third, while the positive peak values are similar at ~1 MA/rad, the location of this peak and the main upward current region differ by more than 2° between the data sets. In Figure 3c, we compare a similarly determined mean profile from 2008 nightside data. The main difference lies within the upward current region, with the Proximal mean I_m profile's gradient being larger and containing clearly negative I_m values at the equatorward boundary, which is not observed in the nightside 2008 profile.

In order to assess the significance of the difference between the means at the same colatitudes for these data sets, we follow the method of Hunt et al. (2018), who applied the Welch's T test. This version of the T test is a robust measure, allowing for the means to have unequal variances and sample sizes. If the T statistic is greater than or equal to 2 and the P values was less than or equal to 0.05, then the null hypothesis that the means are similar can be rejected and the difference between the means is statistically significant, thus giving confidence that the difference is meaningful. The black squares indicate the colatitude bins where the difference in the means passed the T test, principally in Figure 3b spanning the region of negative I_m (i.e., leading field) and equatorward thereof and the equatorward boundary of the nightside auroral current sheet in Figure 3c.

It is important to note that this negative I_m region and extension of the upward field-aligned current of the PPO-independent current system have not been previously observed, as also discussed by Provan et al. (2019). There was no evidence of this in the 2006/2007, 2008 (see Figure 3c), 2012/2013, and F-ring (2016/2017) data sets where similarly determined average profiles were obtained (Bradley et al., 2018; Hunt et al., 2015, 2018). This feature is thus a seemingly unique feature to northern hemisphere Proximal orbit data. As described above, there are clear differences between the average PPO-independent currents determined from the F-ring and the Proximal data sets despite these data being obtained at approximately the same point in Saturn's year, near to northern summer solstice. The major orbital difference between the data sets is the LT, where the Proximal orbits cross the auroral field-aligned currents at ~06–08 hr while the F-ring orbits cross these currents at ~11 hr and 2008 orbits at ~22 hr as shown in Figure 2c. This implies that the enhanced negative I_m, leading azimuthal field, and enhanced upward current are present in the ~06–08 h LT sector but not in the ~10–12 hr nor ~22 hr LT and therefore could be related to the return flows on the dawn flank from reconnection sites down tail (see Figures 2 and 3 of Cowley, Bunce, and Prangé (2004)). To explore the LT difference, we continue by comparing the Proximal with just the F-ring orbits due to similarity in season, as Bradley et al. (2018) and Hunt et al. (2018) showed that seasonal effects could be present in the polar region.

Typical auroral morphology may also help to explain the difference in form and position of the main upward current as determined from the F-ring and Proximal orbits (e.g., Grodent, 2015; Gustin et al., 2017). Recently, Lamy et al., 2018showed using Hubble Space Telescope observations of the northern auroral oval from this time period that the auroral emission was more intense in the dawn sector and that the dawn arc is narrower than in the noon sector (see their Figure 3). They also showed a clear poleward shift of the oval near noon compared to the 06–09 hr LT sector. These auroral morphology and LT displacement are consistent with the form of the averaged field-aligned currents shown in Figure 3 for the F-ring and Proximal data sets.

4. PPO Separation of Northern Meridional Current Profiles

Previous observations of Saturn's northern hemisphere auroral field-aligned current showed minimal PPO-related currents at $\Psi_{N,S} = 0\ ^\circ /360^\circ \& 180^\circ$, maximum PPO-related upward current at $\Psi_{N,S} = 90^\circ$, and maximum PPO-related downward current at $\Psi_{N,S} = 270^\circ$ (Bradley et al., 2018; Hunt et al., 2015, 2018). Ideally, we would also split the data into separate sectors of both Ψ_N and Ψ_S; however, due to Cassini's orbital period and the southern PPO period being approximately linked, data coverage is lacking in key Ψ_S phase sectors. Therefore, here, we only analyze the Ψ_N organization of the data in this statistical way.

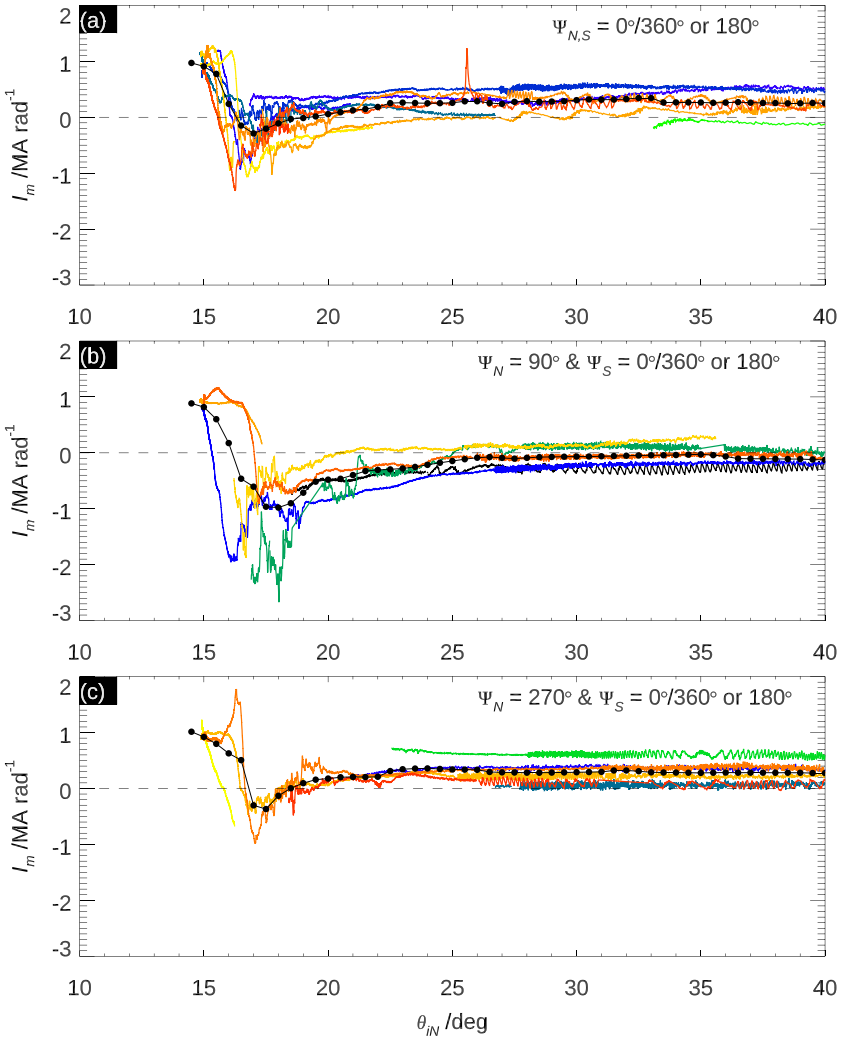

Figure 4. Data separation for the PPO-independent and PPO related current systems. (a–c) Similar format to Figure 3a. Panel (a) shows the colatitudinal I_m profiles for PPO phases ($\Psi_{N,S} = 0^\circ/360^\circ \pm 45^\circ$ and $\Psi_{N,S} = 180^\circ \pm 45^\circ$). These phase sectors are where the northern and southern PPO currents are minimal. Panel (b) shows the colatitudinal I_m profiles for PPO phases where the northern PPO is maximum in the upward direction ($\Psi_N = 90^\circ \pm 45^\circ$) and southern PPO currents are minimal ($\Psi_S = 0^\circ/360^\circ \pm 45^\circ$ and $\Psi_S = 180^\circ \pm 45^\circ$). Panel (c) shows the colatitudinal I_m profiles for PPO phases where the northern PPO is maximum in the downward direction ($\Psi_N = 270^\circ \pm 45^\circ$) and southern PPO currents are minimal ($\Psi_S = 0^\circ/360^\circ \pm 45^\circ$ and $\Psi_S = 180^\circ \pm 45^\circ$).

Figure 4 shows an overview of the PPO separation analysis. To isolate the PPO-independent current, we have selected I_m data that are ±45° of $\Psi_{N,S}$ = 0 ° /360° and 180°. The result of this data selection is shown in Figure 4a in the same format at Figure 3. The average profile here is in excellent agreement with the overall mean profile shown in Figure 3a. To isolate the northern PPO-related upward current contributions, we select data within ±45° of Ψ_N = 90°& Ψ_S = 0 ° /360°or 180°, which is shown in Figure 4b. The effect of the additional PPO-related upward current in this phase sector is evidenced in the larger negative I_m values between θ_{iN}~15° and 20° compared with Figure 4a. The general reduction of I_m equatorward of θ_{iN}~20° is the expected PPO behavior, since, from equation 1, I_m will vary as approximately $-\sin(\Psi_N)$ in the northern hemisphere because B_φ varies as ~$\sin(\Psi_N)$. To isolate the northern PPO-related downward current contributions, we select data within ±45° of Ψ_N = 270° and Ψ_S = 0 ° /360°or 180°, which are shown in Figure 4c. The PPO-related effects are evident in this sector too with the smaller negative values in the overall current region and more positive I_m equatorward of θ_{iN}~20°.

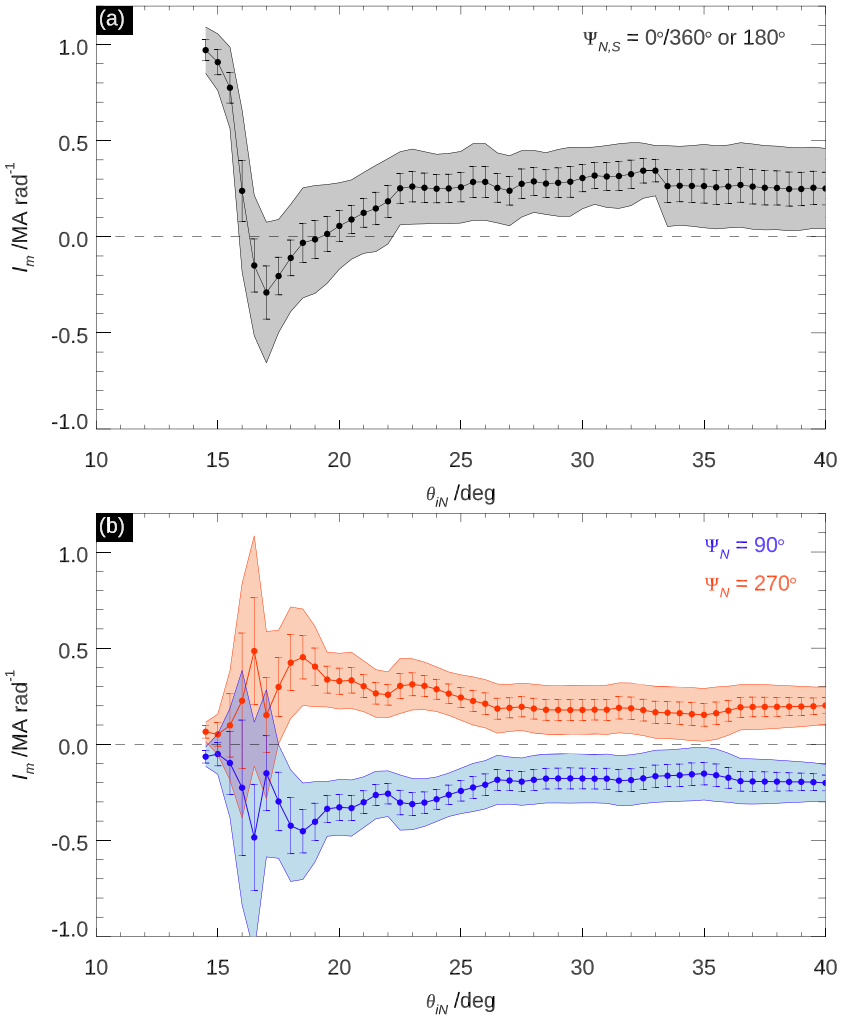

Figure 5. PPO-independent and northern PPO current profiles. Panel (a) shows the average PPO-independent current profile from Figure 4a. The error bars show the standard error of the means and gray shaded region shows a standard deviation. Panel (b) shows the northern PPO system related currents in a similar format to panel (a). The blue profile is the upward current at $\Psi_N = 90^\circ$, while the red profile is for the downward current at $\Psi_N = 270^\circ$.

The separated current system profiles are shown in Figure 5, where in Figure 5a, we show the mean profile from Figure 4a with the associated standard deviation shown by the gray shaded region and the standard error of the means by the error bars. While the selection of the data in Figures 4b and 4c aims to reduce the southern PPO current contribution, the contribution from the PPO-independent current system is still, of course, present in these data. To determine the northern PPO current system explicitly, therefore, we exploit the difference in symmetry between the PPO and PPO-independent systems. To do this, we subtract the two profiles and divide by two, a method first applied to the 2008 data by Hunt et al. (2014). The differencing of the two average profiles from Figures 4b and 4c removes the PPO-independent system, leaving us with the profile of the nonaxisymmetric PPO-related system, assuming that the PPO-related currents are approximately equal and opposite in the two phase sectors selected. The results of this procedure are shown in Figure 5b, where the blue profile corresponds to the $\Psi_N = 90^\circ$ PPO-related current and the red profile to the equal and opposite $\Psi_N = 270^\circ$ downward PPO-related current. The shaded region shows the combined error from the standard deviations of the means shown in Figures 4b and 4c, and the error bars show the combined standard error on the means. The results shown in Figures 5a and 5b are in good agreement with similar profiles from Provan et al. (2019) (see their Figure 19b and Figure 14b), where they obtained mean field profiles from sinusoid fits to colatitudinally binned data. This shows that the results and determined profiles of these currents are robust to details of the applied methodology.

Comparing the separated current profiles in Figures 5a and 5b shows that the peak of the PPO-related current at $\theta_i \sim 16.5°$ lies near the equatorward boundary of the PPO-independent upward current, in agreement with previous observations from earlier in the Cassini mission (Bradley et al., 2018; Hunt et al., 2014, 2015). This observation that the PPO-related currents at a different LT are still found on the equatorward edge of the PPO-independent regardless of the colatitude shift due to the offset of the auroral oval center suggests that there is an intrinsic link between the main upward current of the PPO-independent system and the PPO-related currents. However, the PPO-related currents are seemingly ~50% weaker than the 2008 values (Hunt et al., 2014, 2015), as was also shown by Hunt et al. (2018) to be the case for the F-ring orbits. This could be related to LT dependence of the PPOs' amplitudes as shown by Andrews et al. (2019) and Andrews, Cowley, et al. (2010).

5. Analysis of the Individual Current Sheets

In this section, we turn our attention to the individual current sheets in a given I_m colatitude profile. From inspecting the individual Proximal orbits I_m colatitude profiles shown in Figure 4a, it can be seen that there are typically two large-scale current gradients indicative of field-aligned current sheets. The first is a negative gradient with respect to increasing θ_{iN} associated with the main upward auroral field-aligned current. This is followed by a positive gradient in I_m which is associated with a downward field-aligned current, which partly returns the upward current associated with the leading fields. We identify the boundaries of these current sheets in a similar manner to Hunt et al. (2014, 2016, 2018). At each identified boundary, the current, colatitude, and PPO phase (Ψ_N,Ψ_S) are recorded. For ease of comparison with previous studies, we number these sheets 2 and 3 and the boundaries as 2, 3, and 4. This is the same numbering as used to describe the four-sheet structure of the auroral current (Hunt et al., 2014, 2016, 2018). As described in section 2, due to the Proximal orbit geometry, coverage in the polar region is reduced such that the poleward downward current, sheet 1, is not routinely observed on the Proximal orbit passes. The boundary currents and positions are shown in Figures 6a and 6b as box plots. Here, we show for comparison both Proximal and F-ring field-aligned current sheet properties, where the horizontal line shows the median while stars show the mean values. Figures 6c and 6d show the current across each sheet and its central position, respectively. The colatitudinal width of the sheets are shown in Figure 6e. Finally, in Figure 6f, we show the current densities in both sheets. Here, we have combined the current across the sheets (ΔI_m) shown in Figure 6c and the width of the current sheets ($\Delta\theta_i$) given in Figure 6e. The current densities were then calculated using the following expression:

$$j_{\parallel i} = \frac{\Delta I_m}{R_i^2 \sin\theta_i \Delta\theta_i}. \tag{4}$$

Beginning with the boundaries of the identified current sheets, comparing the values at the boundaries from the Proximal and F-ring orbits shows the differences between the two data sets and LT sectors. In Figure 6a, the poleward boundary of the upward current (Boundary 2) values are approximately the same between the Proximal and F-ring orbits, meaning that the total downward current over the polar region is approximately the same. This is to be expected as both data sets were obtained close to northern summer solstice. However, the current at the equatorward boundary of the upward current (Boundary 3) is at a significantly larger negative I_m value than that at the same boundary during the F-ring orbits. Both the mean and median from the Proximal orbits are outside the middle 50% of the F-ring orbits' current values. Turning to the positions of the current boundaries, the equatorward shift of the field-aligned currents at dawn is evident in the Proximal orbits. In addition, the variation in the position of the upward current boundaries (2 and 3) at dawn during the Proximal data set is lower than for the near-noon F-ring data set. This indicates a steadier upward current at dawn compared with a more variable current near at near noon.

Next, we turn our attention to the properties of the current sheets. The current across the sheet is shown in Figure 6c. The main upward current, Sheet 2, for the Proximal orbits data set shows a distribution of current values that are clearly larger than for the F-ring orbits, with the mean and medians outside the middle 50% of the distribution. This is clear evidence of a larger upward current typically flowing in the main upward auroral current layer at dawn compared with near noon. Once again, the shift by ~2° in colatitudinal position is evident in Figure 6d. The widths of the current sheets are shown in Figure 6e. Examining these shows that

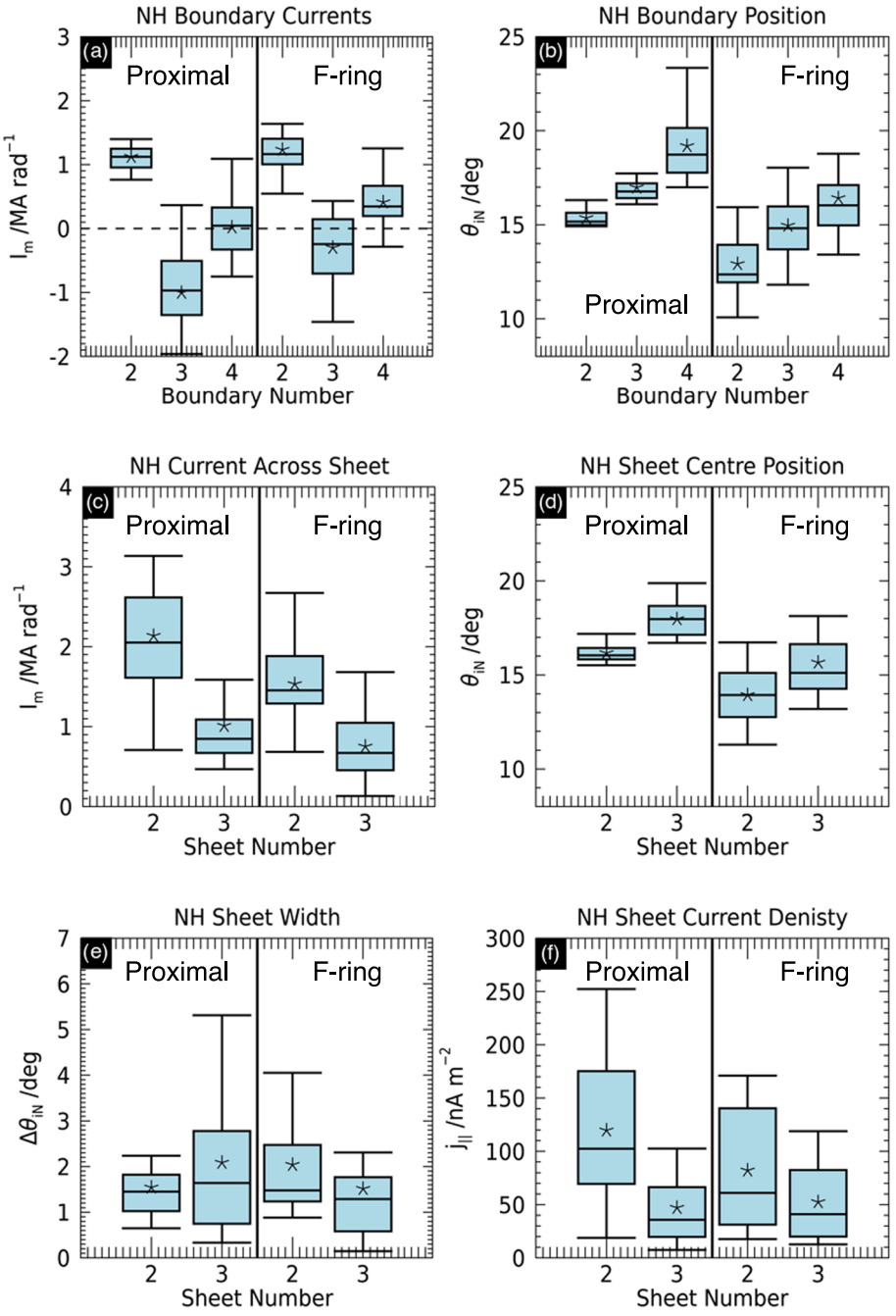

Figure 6. Boxplots of the main field-aligned currents' boundary and sheet properties that were identified from the Proximal and F-ring orbits crossings of the northern auroral field-aligned currents. The properties of the current sheets are shown in each panel (a–f) as titled. The format in each panel is the same, the light blue box is the middle 50% of the distribution of the data, the horizontal line in the box is the median value, the black asterisk is the mean value, and the whiskers show the minimum and maximum values. To the left of the vertical line in each panel are the Proximal orbit properties, while on the right are the F-ring orbit properties.

the upward current width is less variable during the Proximal orbits compared to the F-ring orbits. In addition, the mean width was ~0.5° narrower for the Proximal orbits; these effects were also shown in Figure 3b. Conversely, the downward current shows more variability in width for the Proximal orbit observations, and the mean is ~0.5° wider. Combining the current across the sheet and the current sheet width in equation 4, we also estimate the field-aligned current density just above the ionosphere, shown

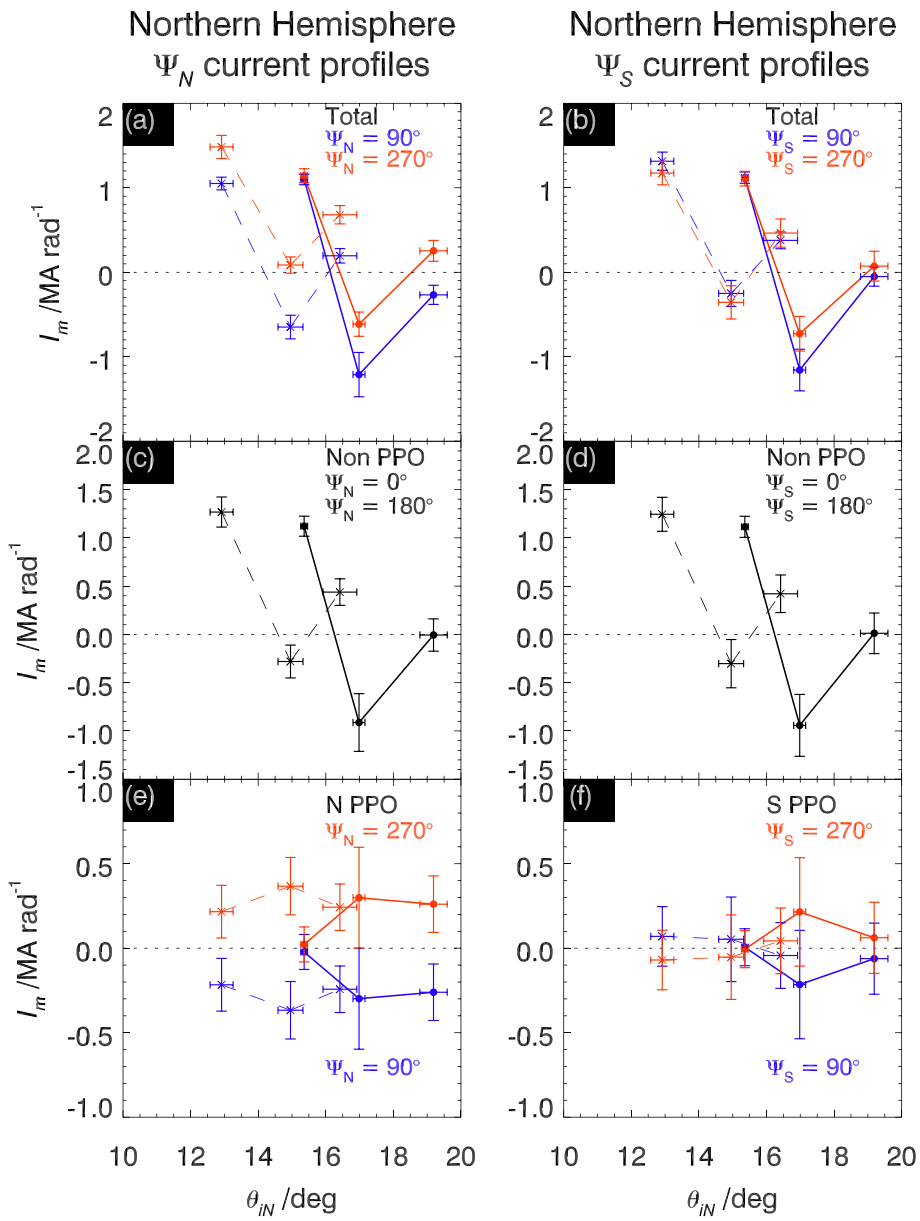

Figure 7. Plots showing the total current profiles (a, b), separated planetary period oscillation (PPO)-independent currents (c, d), and PPO-related currents (e, f). The northern PPO system was used in panels (a), (c), and (e), while the southern PPO system was used in panels (b), (d), and (f). For the total current and PPO-related current profiles, blue is for $\Psi_{N,S}$= 90°, while red is for $\Psi_{N,S}$=270°. The error bars are the standard error of the means in the total current profiles, while they show the combined calculated error in the PPO-independent and PPO-related profiles. The dashed profiles shown here are from the F-ring orbits (Hunt et al., 2018).

in Figure 6f. These box plots show that the mean and median current densities in the dawn upward current sheet are approximately twice the values near to noon.

From the boundary data shown in Figure 6, it is possible to construct mean I_m colatitude profiles of the current sheets. To begin, we organize the I_m values for each boundary by the northern and southern PPO phases, $\Psi_{N,S}$. We sort these I_m data into two 180° bins centered on $\Psi_{N,S}$=90° and $\Psi_{N,S}$=270° and determine the mean I_m values of each bin. These central values are chosen as they are the PPO phase sectors with maximum PPO-related field-aligned currents. We treat each PPO system separately. The resulting profiles for the northern and southern PPO systems are shown in Figures 7a and 7b, respectively. The solid line profiles show the

northern hemisphere Proximal orbit currents, while the dashed lines show the corresponding profiles from the F-ring data as determined by Hunt et al. (2018). The error bars are the standard errors of the mean.

Figure 7 shows that clear difference between the F-ring (dashed) and Proximal (solid) orbits profiles lies in the position and strength of the main upward current. The colatitudinal position near dawn is in full agreement with Hubble Space Telescope UV auroral observations concurrent with Cassini's Proximal orbits for the 06–08 hr LT sector (Lamy et al., 2018). This difference in colatitude between the two LTs implies an oval which is shifted towards the nightside and towards predawn as expected (Carbary, 2012; Nichols et al., 2008). There is, however, a significant difference in the $I_m$values at the equatorward boundary of the main upward current between the F-ring (dashed) and Proximal (solid) profiles, with the latter being ~50% more negative. These profiles are the combination of the PPO-independent and PPO-related current systems. To explore the difference between the current profiles determined from the Proximal and F-ring orbits, we can exploit the difference in symmetry of between the PPO-independent and PPO currents and decompose the total profiles into these components.

To extract the PPO-independent currents, we add the 90° and 270° profiles and divide by 2. This removes the nonaxisymmetric part, the PPO currents. The result of this procedure is shown in Figures 7c and 7d. The PPO-independent profiles are very similar for the two independent data sets regardless of the PPO system used to organize the boundary $I_m$values. This is to be expected, of course, for the currents that are independent of the PPO systems. Here, we see a clear difference between the main upward current F-ring and Proximal orbits. The Proximal orbit profiles extend to a much greater negative $I_m$values compared with the F-ring orbit profiles. As shown in Figure 6c, the mean total current in sheet two is approximately ~1.4 times larger for the Proximal orbits compared to the F-ring orbits, while the sheet width are similar values. Similar profiles were shown by Hunt et al. (2014) for the nightside southern hemisphere PPO-independent currents (see their Figure 14) which also lack the significant negative I_m values at the equatorward boundary of the upward current. To determine the resulting difference in current density, we apply equation 4. For the Proximal (solid) profile, the upward current density is 85.3 nA m^{-2}, while from the F-ring (dash) profile, the current density 59.5 nA m^{-2}, and hence the former is ~1.4 times stronger than the latter, and this is mainly due to an increase in the total current within the upward sheet.

Next, we extract the PPO-related current from the profiles shown in Figures 7a and 7b by subtracting the opposite phase profiles and dividing by two. This removes the axisymmetric PPO-independent current, leaving us with the PPO-related currents shown in Figures 7e and 7f in the same format as Figures 7a and 7b. The northern PPO organization of the current boundaries are clearly present in both data sets with the separation of the blue and red profiles in Figure 7e. The peak current is similar between the F-ring and Proximal orbits observations. We note that also the peak of the PPO-related current is on the equatorial edge of the PPO-independent current systems as previously found in other field-aligned current observations at different LTs (Hunt et al., 2014; Hunt et al., 2016; Hunt et al., 2018). The increase in the $I_m$values at ~17° give potential evidence of the southern PPO system in part organizing the northern field-aligned currents during the Proximal orbits.

In separating the PPO-independent and PPO currents, we have shown that difference between the overall Proximal and F-ring observations shown by the profiles in Figures 7a and 7b is clearly due to the difference in the PPO-independent current and not the PPO currents. In the following section, we will discuss this difference and the implications in more detail.

6. Discussion of the Difference in PPO-Independent Upward Currents

Hunt et al. (2016) derived a proxy for the variation in precipitating electron power per radian of azimuth, and therefore also in auroral emission, due to differences in the properties of the upward current sheets. This proxy is given by

$$P = \frac{\Delta I_m^2}{\sin(\theta_i)\Delta\theta_i}, \tag{5}$$

where ΔI_m is the upward current flowing in the layer, θ_i is ionospheric colatitude at the center of the current sheet, and $\Delta\theta_i$ is the sheet width (with the units MA^2 rad^{-2} deg^{-1}). For the full derivation of

equation 5, see Hunt et al. (2016) (section 4, equations (5)–(12)). Applying equation 5 to the main upward current sheet for the PPO-independent profiles gives a power proxy of ~9.1 for the Proximal profile and ~ 4.9 for the F-ring profile, with the ratio between the two being ~1.9. Considering the LT of the two sets of observations, this implies that the PPO-independent upward current in the dawn sector (06–08 hr) on average has almost twice the precipitating electron power per radian of azimuth compared with the PPO-independent current near noon (10-12 h). This difference in power proxy is approximately consistent with the UV auroral brightness difference between these LT sectors as shown by Lamy et al. (2018) (see their Figure 3). As both sets of observations are from a similar Saturn season, namely, northern summer, we therefore consider this difference to be related to the different LTs of the observations. However, there is an unresolved question here, which is the peak $I_m$values on the F-ring and Proximal orbits, and therefore the proxy power values are approximately half those reported from earlier intervals in the Cassini mission from 2006 to 2008 (Hunt et al., 2016). It is unclear if this difference is due to seasonal, hemispheric, or LT changes.

The difference between the currents at northern dawn and near noon on the Proximal and F-ring orbits, respectively, could arise from a current system associated with the interaction between Saturn's magnetosphere and the solar wind. Such a current system would have downward current in the dusk sector and upward current in the dawn sector (Cowley, Bunce, & Prangé, 2004; Jackman & Cowley, 2006), similar to the "Region 1" and "Region 2" currents observed at Earth (e.g., Cowley, 2000) but opposite in direction due to the opposite polarity of Saturn's planetary field. These currents have been associated with the return flows of the Dungey and Vasyliunas circulation systems via the dawn sector within Saturn's magnetosphere. These currents would flow close to the OCB and would add a dawn-dusk asymmetry to the PPO-independent current system. To date, such a current system has not been observed at Saturn. However, the northern hemisphere PPO-independent current profiles determined from the Proximal orbits through the dawn sector in this paper show the expected enhanced upward current from such a current system when compared with similarly determined profiles from the noon sector. It is therefore possible that the Proximal orbit PPO-independent current profile from the dawn sector have revealed an additional contribution to the upward current from an LT asymmetric current system like that described by Cowley, Bunce and Prangé (2004) and Jackman and Cowley (2006). In order to produce the region of observed leading field, the return flows must make this flow region superotational with respect to the planetary rotation. If so, the variable magnitude of the current pass-to-pass might provide a window into the variable solar wind-dependent flow on the Proximal orbits.

Previously, Hunt et al. (2016) did not find evidence for an LT-dependent contribution when comparing southern hemisphere near dawn-noon and midnight auroral current observations from earlier in the Cassini mission (2006–2008). However, this analysis included a limited number of 13 auroral crossings, four of which were located between 03 and 05 hr, and another six were at a similar prenoon LTs as the F-ring orbit observations. Only two Revs, 30 and 44, were at an LT of ~09 hr. While the return flows from the nightside must be large scale, their effect should be greatest at 03–09 hr, and as this leading field is clearly not present on F-ring orbits at a similar LT to ~50% of the 2006–2008 study. We infer thus that the enhancement of the upward current observed in the dawn PPO-independent current system during the Proximal orbits could be azimuthally extended to be between ~06 and 09 hr and therefore not clearly observed in the Hunt et al. (2016) study due to limited observations in the LT sector. There are implications for the energy input to the upper atmosphere where there are stronger currents fixed in LT at dawn compared to near noon. As this current enhancement appears to be fixed in LT, it could lead to asymmetric heating within the rotating upper atmosphere and auroral region below. Such heating has been proposed as a possible driving source of the twin vortex flows in the upper atmosphere which are thought to generate the PPO-related current systems (Hunt et al., 2014; Jia et al., 2012; Jia & Kivelson, 2012; Smith & Achilleos, 2012; Southwood & Cowley, 2014).

Recently, Bader et al. (2019) used images of the northern aurora from the Cassini's Ultraviolet Imaging Spectrograph to show that the median auroral power has no dawn-dusk asymmetry. They show the "dawn arc" is seemingly a transient signature of large-scale dynamics in the magnetotail, namely, reconnection down tail in the tail current sheet, followed by plasma injection near dawn, which affects the mean auroral power. Here, we show evidence of an increase in upward field-aligned current density at dawn compared

with noon, which is independent of PPO phase. One must be cautious of simply relating current density with auroral emission power. Since Bader et al. (2019) shows that dawn-dusk asymmetry is due to transient signatures of magnetotail reconnection, one would expect that the auroral electron source population will change due to these events, which could lead to a hotter/more tenuous plasma. This was shown by Hunt et al. (2016) to give an increased precipitating energy flux for fixed current parameters. Thus, it could be the case that the enhanced PPO-independent current at dawn combines with a modified source plasma due to transient events associated with magnetotail dynamics. This could result in the powerful auroral dawn arcs and storm events observed at Saturn (e.g., Bader et al., 2019; Clarke et al., 2005; Nichols et al., 2014), energization of plasma in this LT sector (Mitchell et al., 2009), and intense radio emission (e.g. Kurth et al., 2005, 2016; Lamy et al., 2009; Reed et al., 2018).

7. Summary and Conclusions

In this paper, we have analyzed and discussed the northern hemisphere high-latitude auroral currents encountered during Cassini's Proximal orbits. These auroral current sheet crossings occurred in the 06–08 hr LT sector close to the peak in mean SKR and UV auroral power (Lamy et al., 2009). We compared them to observations at the later LT of 10–12 hr obtained during the set of orbits prior to the Proximal orbits, known as the F-ring orbits. We have shown that while the PPO-related currents are similar between the two LT sectors, apart from a shift in latitude, the PPO-independent currents at dawn are noticeably stronger than those near noon.

Using the colatitudinal profiles of the meridional ionospheric currents per radian of azimuthal at the feet of the field lines inferred from the azimuthal magnetic field component, we determined an average profile. The mean profile from the Proximal orbits was shown to be significantly different from a similarly determined profile from the near-noon field-aligned current from the F-ring orbits (Hunt et al., 2018). We exploited the difference in symmetry between the PPO-independent and PPO-related currents to separate them from the overall average meridional current profile. This showed that the key difference was in the PPO-independent current system having a stronger upward current sheet. It is equally important to note that this enhancement in current across the sheet was related specifically to larger negative I_m values at the equatorward boundaries, associated with larger "leading" fields and not larger positive I_m values at the poleward boundaries. The difference in colatitudinal position of the main upward current sheet is also in good agreement with the UV auroral observations of an oval which is displaced towards the nightside (Lamy et al., 2018). The location of the PPO-related current in relation to the PPO-independent current has been shown be to the same as with previous observations from 2006–2008 and 2013 data sets (Bradley et al., 2018; Hunt et al., 2014, 2015, 2018). This suggests that the main PPO-related field-aligned current is linked to the equatorward side of the upward current within the PPO-independent current and that this relationship is maintained as the latitude of the current shifts in LT. This implies an intrinsic link between the PPO-independent and PPO-related current systems.

We identified the main upward current sheet in the individual meridional current profiles. This showed the main upward current sheet to be narrower and stronger at dawn than near noon, resulting, on average, in the current density being ~1.4 times higher at dawn. We also calculated the proxy for precipitating electron power per radian of azimuth from Hunt et al. (2016). This showed that the precipitating power at dawn in the upward PPO-independent current layer is ~1.9 times larger than that near noon.

By comparing the northern hemisphere auroral field-aligned current from the dawn and near-noon sectors observed during the Proximal and F-ring orbits, respectively, we have shown that the dawn PPO-independent upward current sheet is significantly stronger than at near noon. This could be the first direct observational evidence of an LT-dependent auroral current sheet at dawn within Saturn's magnetosphere, similar to that proposed by Cowley et al. (2004) and Jackman and Cowley (2006). The variable magnitude of the current pass-to-pass might provide a window into the variable solar wind-dependent return flow on the Proximal orbits. The enhanced PPO-independent current could combine with changes in source electron properties associated with transient magnetotail dynamics to produce the powerful, intense auroral emissions at dawn. The additional energy input to the auroral region and atmosphere from the fixed LT dawn upward current may play a role in the driving source of atmospheric source of the PPO-related current systems and is worth further investigation.

Acknowledgments

Work at Imperial College was supported by UKRI/STFC grant ST/N000692/1 and ST/S000364/1. Work at the University of Leicester was supported by UKRI/STFC grant ST/N000749/1. E.J.B. was supported by a Royal Society Wolfson Research Merit Award. MKD was funded by Royal Society Research Professorship RP140004. HC was funded by the Cassini project through NASA Jet Propulsion Laboratory (JPL) contract 1579625. Calibrated magnetic field data from the Cassini mission are available from the NASA Planetary Data System (https://pds-ppi.igpp.ucla.edu/search/?sc=Cassini&i=MAG). PPO phase data (2004–2017) are available from the University of Leicester Research Archive (http://hdl.handle.net/2381/42436).

References

Achilleos, N., Arridge, C. S., Bertucci, C., Jackman, C. M., Dougherty, M. K., Khurana, K. K., & Russell, C. T. (2008). Large-scale dynamics of Saturn's magnetopause: Observations by Cassini. *Journal of Geophysical Research*, *113*, A11209. https://doi.org/10.1029/2008JA013265

Andrews, D. J., Cecconi, B., Cowley, S. W. H., Dougherty, M. K., Lamy, L., Provan, G., & Zarka, P. (2011). Planetary period oscillations in Saturn's magnetosphere: Evidence in magnetic field phase data for rotational modulation of Saturn kilometric radiation emissions. *Journal of Geophysical Research*, *116*, A09206. https://doi.org/10.1029/2011JA016636

Andrews, D. J., Coates, A. J., Cowley, S. W. H., Dougherty, M. K., Lamy, L., Provan, G., & Zarka, P. (2010). Magnetospheric period oscillations at Saturn: Comparison of equatorial and high-latitude magnetic field periods with north and south Saturn kilometric radiation periods. *Journal of Geophysical Research*, *115*, A12252. https://doi.org/10.1029/2010JA015666

Andrews, D. J., Cowley, S. W. H., Dougherty, M. K., & Provan, G. (2010). Magnetic field oscillations near the planetary period in Saturn's equatorial magnetosphere: Variation of amplitude and phase with radial distance and local time. *Journal of Geophysical Research*, *115*, A04212. https://doi.org/10.1029/2009JA014729

Andrews, D. J., Cowley, S. W. H., Provan, G., Hunt, G. J., Hadid, L. Z., Morooka, M. W., & Wahlund, J. -E. (2019). The structure of planetary period oscillations in Saturn's equatorial magnetosphere: Results from the Cassini Mission. *Journal of Geophysical Research: Space Physics*, *124*, 8361–8395. https://doi.org/10.1029/2019JA026804

Bader, A., Badman, S. V., Cowley, S. W. H., Yao, Z. H., Ray, L. C., Kinrade, J., et al. (2019). The dynamics of Saturn's main aurorae. *Geophysical Research Letters*, *46*, 10,283–10,294. https://doi.org/10.1029/2019GL084620

Bader, A., Badman, S. V., Kinrade, J., Cowley, S. W. H., Provan, G., & Pryor, W. R. (2018). Statistical planetary period oscillation signatures in Saturn's UV auroral intensity. *Journal of Geophysical Research: Space Physics*, *123*, 8459–8472. https://doi.org/10.1029/2018JA025855

Badman, S. V., Andrews, D. J., Cowley, S. W. H., Lamy, L., Provan, G., Tao, C., et al. (2012). Rotational modulation and local time dependence of Saturn's infrared H 3 + auroral intensity. *Journal of Geophysical Research*, *117*, A09228. https://doi.org/10.1029/2012JA017990

Bradley, T. J., Cowley, S. W. H., Provan, G., Hunt, G. J., Bunce, E. J., Wharton, S. J., et al. (2018). Field-aligned currents in Saturn's nightside magnetosphere: Subcorotation and planetary period oscillation components during northern spring. *Journal of Geophysical Research: Space Physics*, *123*, 3602–3636. https://doi.org/10.1029/2017JA024885

Bunce, E. J., Arridge, C. S., Clarke, J. T., Coates, A. J., Cowley, S. W. H., Dougherty, M. K., et al. (2008). Origin of Saturn's aurora: Simultaneous observations by Cassini and the Hubble Space Telescope. *Journal of Geophysical Research*, *113*, A09209. https://doi.org/10.1029/2008JA013257

Bunce, E. J., Cowley, S. W. H., Alexeev, I. I., Arridge, C. S., Dougherty, M. K., Nichols, J. D., & Russell, C. T. (2007). Cassini observations of the variation of Saturn's ring current parameters with system size. *Journal of Geophysical Research*, *112*, A10202. https://doi.org/10.1029/2007JA012275

Cao, H., Dougherty, M. K., Hunt, G. J., Provan, G., Cowley, S. W. H., Bunce, E. J., et al. (2019). The landscape of Saturn's internal magnetic field from the Cassini Grand Finale. *Icaraus*, 113541. https://doi.org/10.1016/j.icarus.2019.113541

Carbary, J. F. (2012). The morphology of Saturn's ultraviolet aurora. *Journal of Geophysical Research*, *117*, A06210. https://doi.org/10.1029/2012JA017670

Carbary, J. F., & Mitchell, D. G. (2013). Periodicities in Saturn's magnetosphere. *Reviews of Geophysics*, *51*, 1–30. https://doi.org/10.1002/rog.20006

Clarke, J. T., Gérard, J. C., Grodent, D., Wannawichian, S., Gustin, J., Connerney, J., et al. (2005). Morphological differences between Saturn’s ultraviolet aurorae and those of Earth and Jupiter. *Nature*, *433*, 717–719. https://doi.org/10.1038/nature03331

Cowley, S. W. H. (2000). Magnetospheric current systems. *Geophysical Monograph Series*, *118*. https://doi.org/10.1029/GM118

Cowley, S. W. H., Arridge, C. S., Bunce, E. J., Clarke, J. T., Coates, A. J., Dougherty, M. K., et al. (2008). Auroral current systems in Saturn's magnetosphere: Comparison of theoretical models with Cassini and HST observations. *Annales Geophysicae*, *26*(9), 2613–2630. https://doi.org/10.5194/angeo-26-2613-2008

Cowley, S. W. H., Bunce, E. J., & O'Rourke, J. M. (2004). A simple quantitative model of plasma flows and currents in Saturn's polar ionosphere. *Journal of Geophysical Research*, *109*, A05212. https://doi.org/10.1029/2003JA010375

Cowley, S. W. H., Bunce, E. J., & Prangé, R. (2004). Saturn's polar ionospheric flows and their relation to the main auroral oval. *Annales Geophysicae*, *22*(4), 1379–1394. https://doi.org/10.5194/angeo-22-1379-2004

Dougherty, M. K., Kellock, S., Southwood, D. J., Balogh, A., Smith, E. J., Tsurutani, B. T., et al. (2004). The Cassini magnetic field investigation. *Space Science Reviews*, *114*(1–4), 331–383. https://doi.org/10.1007/s11214-004-1432-2

Dougherty, M. K., Cao, H., Khurana, K. K., Hunt, G. J., Provan, G., Kellock, S., et al. (2018). Saturn's magnetic field revealed by the Cassini Grand Finale. *Science*, *362*(6410). https://doi.org/10.1126/science.aat5434

Grodent, D. (2015). A brief review of ultraviolet auroral emissions on giant planets. *Space Science Reviews*, *187*(1–4), 23–50. https://doi.org/10.1007/s11214-014-0052-8

Gurnett, D. A., Lecacheux, A., Kurth, W. S., Persoon, A. M., Groene, J. B., Lamy, L., et al. (2009). Discovery of a north-south asymmetry in Saturn's radio rotation period. *Geophysical Research Letters*, *36*, L16102. https://doi.org/10.1029/2009GL039621

Gustin, J., Grodent, D., Radioti, A., Pryor, W., Lamy, L., & Ajello, J. (2017). Statistical study of Saturn's auroral electron properties with Cassini/UVIS FUV spectral images. *Icarus*, *284*, 264–283. https://doi.org/10.1016/j.icarus.2016.11.017

Hunt, G. J., Cowley, S. W. H., Provan, G., Bunce, E. J., Alexeev, I. I., Belenkaya, E. S., et al. (2014). Field-aligned currents in Saturn's southern nightside magnetosphere: Subcorotation and planetary period oscillation components. *Journal of Geophysical Research: Space Physics*, *119*, 9847–9899. https://doi.org/10.1002/2014JA020506

Hunt, G. J., Cowley, S. W. H., Provan, G., Bunce, E. J., Alexeev, I. I., Belenkaya, E. S., et al. (2015). Field-aligned currents in Saturn's northern nightside magnetosphere: Evidence for interhemispheric current flow associated with planetary period oscillations. *Journal of Geophysical Research: Space Physics*, *120*, 7552–7584. https://doi.org/10.1002/2015JA021454

Hunt, G. J., Cowley, S. W. H., Provan, G., Bunce, E. J., Alexeev, I. I., Belenkaya, E. S., et al. (2016). Field-aligned currents in Saturn's magnetosphere: Local time dependence of southern summer currents in the dawn sector between midnight and noon. *Journal of Geophysical Research: Space Physics*, *121*, 7785–7804. https://doi.org/10.1002/2016JA022712

Hunt, G. J., Cowley, S. W. H., Provan, G., Cao, H., Bunce, E. J., Dougherty, M. K., & Southwood, D. J. (2019). Currents associated with Saturn's intra-D ring azimuthal field perturbations. *Journal of Geophysical Research: Space Physics*, *124*, 5675–5691. https://doi.org/10.1029/2019JA026588

Hunt, G. J., Provan, G., Bunce, E. J., Cowley, S. W. H., Dougherty, M. K., & Southwood, D. J. (2018). Field-aligned currents in Saturn's magnetosphere: Observations from the F-ring orbits. *Journal of Geophysical Research: Space Physics*, *123*, 3806–3821. https://doi.org/10.1029/2017JA025067

Jackman, C. M., & Cowley, S. W. H. (2006). A model of the plasma flow and current in Saturn's polar ionosphere under conditions of strong Dungey cycle driving. *Annales Geophysicae*, *24*(3), 1029–1055. https://doi.org/10.5194/angeo-24-1029-2006

Jasinski, J. M., Arridge, C. S., Bader, A., Smith, A. W., Felici, M., Kinrade, J., et al. (2019). Saturn's open-closed field line boundary: A Cassini electron survey at Saturn's magnetosphere. *Journal of Geophysical Research: Space Physics*, *124*, 10,018–10,035. https://doi.org/10.1029/2019JA027090

Jia, X., & Kivelson, M. G. (2012). Driving Saturn's magnetospheric periodicities from the upper atmosphere/ionosphere: Magnetotail response to dual sources. *Journal of Geophysical Research*, *117*, A11219. https://doi.org/10.1029/2012JA018183

Jia, X., Kivelson, M. G., & Gombosi, T. I. (2012). Driving Saturn's magnetospheric periodicities from the upper atmosphere/ionosphere. *Journal of Geophysical Research*, *117*, A04215. https://doi.org/10.1029/2011JA017367

Khurana, K. K., Dougherty, M. K., Provan, G., Hunt, G. J., Kivelson, M. G., Cowley, S. W. H., et al. (2018). Discovery of atmospheric-wind-driven electric currents in Saturn's magnetosphere in the gap between Saturn and its rings. *Geophysical Research Letters*, *45*, 10,068–10,074. https://doi.org/10.1029/2018GL078256

Kinrade, J., Badman, S. V., Provan, G., Cowley, S. W. H., Lamy, L., & Bader, A. (2018). Saturn's northern auroras and their modulation by rotating current systems during late northern spring in early 2014. *Journal of Geophysical Research: Space Physics*, *123*, 6289–6306. https://doi.org/10.1029/2018JA025426

Kurth, W. S., Gurnett, D. A., Clarke J. T., Zarka, P., Desch, M. D., Kaiser, M. L., et al. (2005). An Earth-like correspondence between Saturn’s auroral features and radio emission. *Nature*, *433*(7027), 722–725. https://doi.org/10.1038/nature03334 Kurth, W. S., Hospodarsky, G. B., Gurnett, D. A., Lamy, L., Dougherty, M. K., Nichols, J. et al. (2016). Saturn kilometric radiation intensities during the Saturn auroral campaign of 2013. *Icarus*, *263*, 2–9. https://doi.org/10.1016/j.icarus.2015.01.003

Lamy, L., Cecconi, B., Prangé, R., Zarka, P., Nichols, J. D., & Clarke, J. T. (2009). An auroral oval at the footprint of Saturn's kilometric radio sources, colocated with the UV aurorae. *Journal of Geophysical Research*, *114*, A10212. https://doi.org/10.1029/2009JA014401

Lamy, L., Prangé, R., Tao, C., Kim, T., Badman, S. V., Zarka, P., et al. (2018). Saturn's northern aurorae at solstice from HST observations coordinated with Cassini's grand finale. *Geophysical Research Letters*, *45*, 9353–9362. https://doi.org/10.1029/2018GL078211

Mitchell, D. G., Krimigis, S. M., Paranicas, C., Brandt, P. C., Carbary, J. F., Roelof, E. C., et al. (2009). Recurrent energization of plasma in the midnight-to-dawn quadrant of Saturn's magnetosphere, and its relationship to auroral UV and radio emissions. *Planetary and Space Science*, *57*(14–15), 1732–1742. https://doi.org/10.1016/j.pss.2009.04.002

Nichols, J. D., Cecconi, B., Clarke, J. T., Cowley, S. W. H., Gérard, J. C., Grocott, A., et al. (2010). Variation of Saturn's UV aurora with SKR phase. *Geophysical Research Letters*, *37*, L15102. https://doi.org/10.1029/2010GL044057

Nichols, J. D., Clarke, J. T., Cowley, S. W. H., Duval, J., Farmer, A. J., Gérard, J.-C., Grodent, D., & Wannawichian, S. (2008). Oscillation of Saturn's southern auroral oval. *Journal of Geophysical Research*., *113*, A11205. https://doi.org/10.1029/2008JA013444

Nichols, J. D., V.Badman, S., Baines, K. H., Brown, R. H., Bunce, E. J., Clarke, J. T., et al. (2014). Dynamic auroral storms on Saturn as observed by the Hubble Space Telescope. *Geophysical Research Letters*, *41*, 3323–3330. https://doi.org/10.1002/2014GL060186

Provan, G., Andrews, D. J., Arridge, C. S., Coates, A. J., Cowley, S. W. H., Milan, S. E., et al. (2009). Polarization and phase of planetary-period magnetic field oscillations on high-latitude field lines in Saturn's magnetosphere, *Journal of Geophysical Research*., *114*, A02225. https://doi.org/10.1029/2008JA013782

Provan, G., Cowley, S. W. H., Bradley, T. J., Bunce, E. J., Hunt, G. J., & Dougherty, M. K. (2018). Planetary period oscillations in Saturn's magnetosphere: Cassini magnetic field observations over the northern summer solstice interval. *Journal of Geophysical Research: Space Physics*, *123*, 3859–3899. https://doi.org/10.1029/2018JA025237

Provan, G., Cowley, S. W. H., Bunce, E. J., Bradley, T. J., Hunt, G. J., Cao, H., & Dougherty, M. K. (2019). Variability of intra–D ring azimuthal magnetic field profiles observed on Cassini's proximal periapsis passes. *Journal of Geophysical Research: Space Physics*, *124*, 379–404. https://doi.org/10.1029/2018JA026121

Reed, J. J., Jackman, C. M., Lamy, L., Kurth, W. S., & Whiter, D. K. (2018). Low-frequency extensions of the Saturn Kilometric Radiation as a proxy for magnetospheric dynamics. *Journal of Geophysical Research: Space Physics*, *123*, 443–463. https://doi.org/10.1002/2017JA024499

Smith, C. G. A., & Achilleos, N. (2012). Axial symmetry breaking of Saturn's thermosphere. *Monthly Notices of the Royal Astronomical Society*, *422*(2), 1460–1488. https://doi.org/10.1111/j.1365-2966.2012.20719.x

Southwood, D. J., & Cowley, S. W. H. (2014). The origin of Saturn's magnetic periodicities: Northern and southern current systems. *Journal of Geophysical Research: Space Physics*, *119*, 1563–1571. https://doi.org/10.1002/2013JA019632

Southwood, D. J., & Kivelson, M. G. (2007). Saturnian magnetospheric dynamics: Elucidation of a camshaft model. *Journal of Geophysical Research*, *112*, A12222. https://doi.org/10.1029/2007JA012254

Sulaiman, A. H., Kurth, W. S., Hospodarsky, G. B., Averkamp, T. F., Ye, S. Y., Menietti, J. D., et al. (2018). Enceladus Auroral hiss emissions during Cassini's grand finale. *Geophysical Research Letters*, *45*, 7347–7353. https://doi.org/10.1029/2018GL078130

Talboys, D. L., Arridge, C. S., Bunce, E. J., Coates, A. J., Cowley, S. W. H., & Dougherty, M. K. (2009a). Characterization of auroral current systems in Saturn's magnetosphere: High-latitude Cassini observations. *Journal of Geophysical Research*, *114*, A06220. https://doi.org/10.1029/2008JA013846

Talboys, D. L., Arridge, C. S., Bunce, E. J., Coates, A. J., Cowley, S. W. H., Dougherty, M. K., & Khurana, K. K. (2009b). Signatures of field-aligned currents in Saturn's nightside magnetosphere. *Geophysical Research Letters*, *36*, L19107. https://doi.org/10.1029/2009GL039867

Talboys, D. L., Bunce, E. J., Cowley, S. W. H., Arridge, C. S., Coates, A. J., & Dougherty, M. K. (2011). Statistical characteristics of field-aligned currents in Saturn's nightside magnetosphere. *Journal of Geophysical Research*, *116*, A04213. https://doi.org/10.1029/2010JA016102